Wall-pressure fluctuations of laminar separation bubble based on direct numerical simulation and experiments over a hydrofoil at Re = 450,000

Antoine Ducoin, J.A. Astolfi

Wall-pressure fluctuations of Laminar Separation Bubble based on Direct Numerical Simulation and Experiments over a Hydrofoil at Re=450,000

A. Ducoin[a], J. A. Astolfi[b]

[a] *LHEEA laboratory, Ecole Centrale de Nantes (CNRS UMR 6598), 44300 Nantes, France*

[b] *Institut de Recherche de l'Ecole Navale EA 3634, Ecole Navale, 29240 Brest Cedex 9, France*

Abstract

The objective of this paper is to investigate wall-pressure fluctuations downstream of a Laminar Separation Bubble (LSB) on a laminar NACA66 hydrofoil section, based on Direct Numerical Simulation (DNS) and experimental analysis. DNS is performed using the massively parallelized open source code Nek5000, which uses the high order spectral element method to solve the incompressible Navier-Stokes equations. It is compared to measurements performed in a hydrodynamic tunnel at the French Naval Academy Research Institute (IRENav). A Reynolds numbers of $Re = 450,000$ with an angle of attack of $\alpha = 4°$ is considered, which induces an LSB to the rear of the maximum thickness of the boundary layer. The local wall pressures at three different locations are compared: just downstream of the LSB at x/c=0.7, in the breakdown region of the LSB at x/c=0.8 and in the fully turbulent region at x/c=0.9. The DNS results compare very well with the measured wall pressures. The DNS captures efficiently the periodic fluctuations downstream of the LSB, up to the random behavior induced by the

*corresponding author
antoine.ducoin@ec-nantes.fr

transition to turbulence. Analysis of the boundary layer flow obtained by DNS suggests that an H-type or K-type transition occurs, characterized by 2D TS waves and typical Λ structures, that break down and generate turbulence. Moreover, it shows that intense and localized pressure fluctuations occur in the breakdown region.
Key words: laminar separation bubble, wall pressure fluctuation, transition, laminar propeller section, spectral element method

1. Introduction

For many marine applications operating at low angles of attack, laminar profiles can be chosen for the propeller blade in order to reduce friction at the body surface and hence improve performance. However, this leads to development of further transitional regimes, even at high Reynolds numbers where the boundary layer is usually considered to be fully turbulent. These transitional regimes can induce large pressure fluctuations and hence wide variation in the hydrodynamic loadings. Hence, numerical and experimental investigations are still necessary to help predict performance in the context of marine propeller sizing. Moreover, the present study can help to improve the physical understanding of (i) cavitation inception at the blade surface, which is known to occur inside Laminar Separation Bubbles (LSB) in the case of transitional flows, and (ii) laminar separation-induced structural vibrations.

Typically, this type of transition occurs at low to moderate Reynolds numbers and is triggered by a laminar separation and a reversed flow, caused by an adverse pressure gradient. The development of the turbulent flow induces

a momentum transfer in the direction normal to the wall, which reattaches the flow. An LSB or transitional separation bubble is then generated ([16]), which is characterized by a dead region near the laminar separation, and an unstable region near the reattachment point. This point is usually subjected to a low frequency oscillation in the shear layer (known as *flapping*), which is responsible for the first destabilization of the LSB. Meanwhile, it has been shown that primary instabilities (Kelvin-Helmholtz vortex and/or Tollmien-Schlichting waves) lead to LSB vortex shedding. Upstream of the LSB, the flow is highly unstable and is governed by complex mechanisms identified as primary and secondary instabilities that lead to transition to turbulence.

The physical understanding of laminar to turbulent transition over lifting profiles is derived primarily from aerodynamic applications on small-scale devices, where the transition comprises a large portion of the chord and dominates the boundary layer flow. The associated Reynolds numbers are typically in the range $20,000 < Re < 100,000$. In order to study the transition to turbulence at these high Reynolds numbers, DNS studies of transitional flows were introduced approximately a decade ago, supported by experimental observations. It has been shown both experimentally [17] and numerically [22] that the transitional region appears near the trailing edge for low to moderate angles of attack, and moves towards the leading edge as the angle of attack increases. The transition on the SD7003 geometry has been extensively investigated for Reynolds numbers in the range $20000 < Re < 66000$, and for different angles of attack using experimental [3, 40, 30, 29] and numerical methods [39, 38]. At $Re = 20000$, transition is observed near the

trailing edge and a vortex associated with a Kelvin-Helmholtz instability is convected into the foil's wake, which strongly interacts with the well-known von Kármán instability. In [13], the characteristic frequency of LSB vortex shedding matches the Strouhal number found in the work of [33], defined for a flat plate with a pressure gradient. For $Re = 66000$, transition is stronger and a burst phenomenon is associated with a fast transition to turbulence [3, 39], although Kelvin-Helmholtz instabilities may still be observed. Jones et al. [21] performed a numerical analysis of an LSB in the case of an airfoil at $\alpha = 5°$ with a low Reynolds number, $Re = 50000$. The authors investigated the instability mechanisms leading to the breakdown to turbulence, linking the breakdown to the combination of two absolute instabilities: an elliptic instability and a mode-B or hyperbolic instability. An important conclusion was that, in the absence of a convectively driven transition effect within the shear layer, an absolute instability can take place, weakening the influence of free stream turbulence. More recently, an interesting DNS study investigated the effect of aspect ratio on laminar to turbulent transition on a NACA0012 profile ([41]). Due to computational costs, the simulation used a reduced span and periodic boundary conditions. The results suggest that different aspect ratios result in close predictions of the time-averaged aerodynamic quantities, although small aspect ratios tend to under-predict the turbulent fluctuations near the separation point but over-predict them inside the separation bubble. This work highlighted the importance of setting span length correctly to predict the development of turbulence. However, the effect of aspect ratio on the initial development of coherent structures downstream from the LSB has not been investigated.

The NACA4412 airfoil profile has also been extensively investigated, mainly for wind turbine applications. In the experiments of [26], the location and formation of LSB were affected both by Reynolds number (ranging from $Re = 25,000$ to $Re = 50,000$) and angle of attack. Moreover, the near wake seems to be affected by LSB and trailing-edge separation, as also observed by [13]. This profile has been also investigated numerically for aircraft applications involving a much higher Reynolds number, $Re = 400,000$ [19]. The authors use the spectral element code NEK5000, and set over 3.2 billion grid points, with an element order of 12 and a full domain. This work showed the ability of the spectral element method to predict the transition and the development of turbulence. The authors also showed that adverse pressure gradients have a great influence on the development of the boundary layer and turbulent kinetic energy.

As far as hydrodynamic applications are concerned, very few papers have addressed the prediction of transitional flows on marine propellers. Those that do usually use RANS based codes with empirical transition models, and hence no LSB dynamic is captured. In [2], the authors show that the use of a transition model leads to an improvement in the flow pattern and slight increases in thrust. However, prediction of the transition location is strongly dependent on the values for turbulence inlet used by the model. [34] investigated how application of a transition model inuences the flow prediction for a cavitating marine propeller. The results clearly correlated cavitation inception with the location of transitional regions, however, conclusions could not be drawn concerning the influence of transition modeling on cavitation de-

velopment and global propeller performance. Similar conclusions are drawn in [14]. More academically, experimental studies on LSB have been carried out on marine propeller sections (i.e. hydrofoils) at the Naval Academy Research Institute (IRENav), France. Several of these studies concerned the NACA66 section, for which highly transitional flows have been observed for relatively high Reynolds numbers (Re=300,000 to 1,000,000). It has been shown that a very strong and localized transition to turbulence occurs inside the boundary layer, which induces intense pressure fluctuations ([11]) that strongly influence hydrodynamic performance [8]. Moreover, it has been demonstrated that this type of transition induces important structural vibrations. [12] showed that there could be a strong interaction between these vibrations and the physics of LSB vortex shedding. In particular, additional frequencies close to that of LSB shedding and structural modes were observed in the vibration spectra in transitional flows, as well as a global increase in amplitude, which could be the result of a complex fluid structure interaction phenomenon. This work also showed that when the frequency of LSB vortex shedding approaches a natural vibration mode, resonance with the natural frequencies of the blade can be obtained and additional harmonics of the main LSB shedding frequency are observed. It should be noted that this behaviour is quite different from that of transition-induced vibrations on membrane wings, which is a major field of investigation of transition-induced vibration. The latter case is characterized by much lower Reynolds numbers and large deformations of the structure, which is seen to significantly change the LSB characteristics [9]. Moreover, the laminar profiles of a marine propeller are obtained by moving the maximum thickness to the center of the

chord, which reduces the adverse pressure gradient and hence increases the critical Reynolds number of transition, Re_θ, see Figure 1. This results in a delay of transition compared with conventional, non-laminar profiles, and a modification of the Re_θ slope after transition occurs, which can induce different physical processes compared to existing aerodynamic studies.

Finally, although a link between LSBs and cavitation inception has been clearly identified by John Carlton in his book about marine propellers [5], it remains poorly understood. It is known that the effect of LSB strongly depends on the scale of the propeller, its surface roughness and the nuclei density. For a model scale with low surface roughness, the position of cavitation inception is related to the transition point, i.e. the location of the LSB. For high angles of attack (before stall), cavitation germs may be trapped inside the LSB to form cavitation patches at the leading edge. Further development of these patches typically results in sheet cavitation. In [1], the authors studied cavitation on a two-dimensional Eppler hydrofoil. They found some indication of the presence of a separation bubble through pressure measurements. At the suction side, a region with a near-constant pressure aft of the pressure peak was observed, and cavitation inception is observed as a band along the leading edge, similar to the type of inception associated with laminar separation. Moreover, examination of the spanwise vorticity indicates a thin region of vorticity production which could be an additional indicator of the presence of a thin leading edge flow separation, where cavitation appears.

For lower angles of attack, the LSB is located from the mid-chord up to the

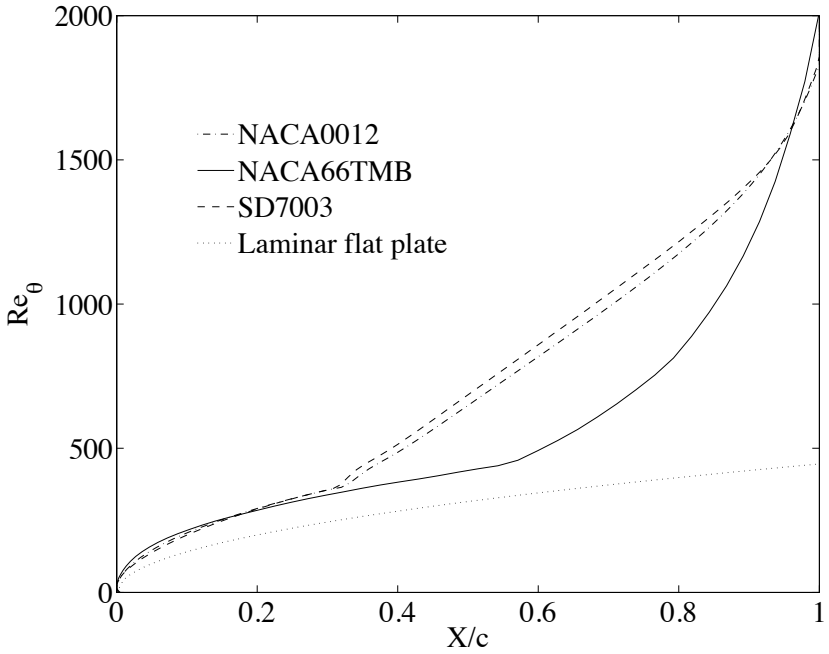

Figure 1: Critical Reynolds number Re_θ along the chord obtained with Xfoil. Comparison of laminar (NACA66) and non-laminar (NACA0012 and sd7003) profiles at $Re = 450,000$.

trailing edge, depending on the inflow conditions and hydrofoil geometry, and cavitation typically occurs in this region, which is mainly correlated with the adverse pressure gradient and the location of minimum pressure. Because there is no negative pressure peak, bubbles can grow and form cavitation bubbles, which appear quite randomly around the minimum pressure at the surface. As a consequence, further studies investigating the link between LSB, wall pressure and cavitation are essential.

Therefore, the objective of the present work is to characterize the wall pressure downstream from an LSB on a laminar NACA66 section operat-

ing at a low angle of attack and at $Re = 450,000$, through a combination of numerical and experimental analysis. Because of the moderate Reynolds number considered, a simplified DNS domain is used and RANS velocity profiles are implemented for the inflow conditions. A mesh sensitivity analysis was first carried out at a lower Reynolds number ($Re = 225,000$), and a similar resolution is used for the target Reynolds number ($Re = 450,000$) by increasing the elements order. To check the validity of the model, mean flow is compared with the RANS calculation. Then, the wall pressure fluctuations are investigated both experimentally and numerically at three different locations between the LSB and the fully turbulent boundary layer. Finally, the flow is analyzed numerically, and conclusions are drawn concerning the particularity of bubble dynamics and its effects on wall pressure fluctuations over laminar hydrofoil sections.

2. Experimental method

Measurements were carried out in the cavitation tunnel at IRENav, France. The test section was 1 m long with a $h = 0.192$ m square section. The velocity ranged between 0 and 15m/s and the pressure from 30 mbar to 3bars. The hydrofoil was a NACA 66 with a NACA a=0.8 camber type, a camber ratio of 2% and a relative thickness of 12% [27]. It was mounted horizontally in the tunnel test section. The chord was $c = 0.150$m and the span is $b = 0.191$m, yielding a low aspect ratio $b/c = 1.3$ and a confinement parameter $h/c = 1.28$. Flow visualizations show that about 80 to 90% of the foil surface could be considered to be 2D flow ([27]), depending on the angle of

incidence.

Pressure measurements were carried out using seventeen piezo-resistive transducers (Keller AG 2 MI PAA100-075-010) of 10 bars maximum pressure. The pressure transducers were mounted into small cavities with a 0.5 mm diameter pinhole at the hydrofoil surface. The wall pressure spectrum measured by the transducer was attenuated at the theoretical cut-off frequency $f_c = 9152$Hz. Experiments used a sample frequency of $f = 20$kHz. A main set of ten transducers was aligned along the chord on the suction side at mid-span, where the flow was considered to be quasi-2D: from the leading edge, at the reduced coordinate $x/c = 0.1$, to the trailing edge, at coordinate $x/c = 0.90$, with a step of 0.10c.

Measurements were performed using an angle of attack $\alpha = 4^\circ$ and upstream velocities ranging from $U_\infty = 1.5$ m/s to 10m/s, corresponding to Reynolds numbers ranging from $Re = 225,000$ to $1,500,000$. Under these conditions, laminar flow was maintained over about 60% to 80% of the chord and hence pressure fluctuations were observed starting at $x/c = 0.7$. It was also observed that the signal to noise ratio leads to accurate measurements of the physical pressure fluctuations for $U_\infty \geq 3$ m/s, i.e. $Re \geq 450,000$.

3. Computational methods

3.1. Direct Numerical Simulation

The dynamics of a three-dimensional incompressible flow of a Newtonian fluid are described by the Navier-Stokes equations:

$$\begin{aligned} \dot{\mathbf{U}} &= -(\mathbf{U}\cdot\nabla)\mathbf{U} - \nabla P + Re^{-1}\Delta\mathbf{U} \\ \nabla\cdot\mathbf{U} &= 0 \end{aligned} \tag{1}$$

where $\mathbf{U} = (U_x, U_y, U_z)^T$ is the velocity vector and P the pressure term. The Reynolds number is defined by $Re = U_\infty c/\nu$, where ν is the kinematic viscosity of the considered fluid, c is the chord length and U_∞ is the upstream velocity.

The Navier-Stokes equations were solved using the flow solver Nek5000 developed at Argonne National Laboratory by Fischer et al. [15]. The method is based on the spectral elements method (SEM), introduced by Patera [32], which provides spectral accuracy in space while allowing for the geometrical flexibility of finite element methods. Spatial discretization is obtained by decomposing the physical domain into spectral elements within which the velocity is defined on Gauss-Lobatto-Legendre (GLL) nodes and the pressure field on Gauss-Legendre (GL) nodes. The solution to the Navier-Stokes equations is then approximated within each element as a sum of Lagrange interpolants defined by an orthogonal basis of Legendre polynomials up to degree N. The results presented in this paper were obtained with a polynomial order from $N = 8$ to $N = 12$. The convective terms were advanced in time using an extrapolation of order 3, whereas the viscous terms used a

backward differentiation, also of order 3, resulting in the time-advancement scheme labeled BDF3/EXT3. Nek5000 employs the MPI standard for parallelism [36, 37]. For further details about the spectral element method, the reader is referred to the books by [10] and [24]. The calculations were performed on the French National Server named Institute for Development and Resources in Intensive Scientific Computing (IDRIS). IBM Blue Gene/Q was the super computer used, which has high energy efficiency of 2.17 Gflops/W. The main characteristics of this machine include six racks, each having 1024 nodes and a total of 98,304 cores with 1GB per core.

The scalability of Nek5000 was tested with the present case up to 32768 processors and 326 million grid points, and compared with a combustion case with the same code, using a blue Gene/P ([25]), see Figure 2. The results show a large decrease in computing efficiency when the ratio between the number of grid points N and the number of processors P decreases below 20000. To achieve an efficiency greater than 90%, the following number of processors were chosen for the simulations: $P = 16384$ at order O(12), $P = 8192$ at order O(10) and $P = 2048$ at order O(8).

3.2. Numerical setup

Because of the moderate Reynolds number considered for DNS ($Re = 450,000$), the DNS domain was restricted to the near wall region, and velocity boundary conditions were imposed at the domain inlet boundaries (left, top and bottom regions) from a transitional RANS calculation to reproduce the velocity gradient external to the hydrofoil boundary layer, see Figure 3. $\nabla \mathbf{U} \cdot \mathbf{x} = 0$ was set at the outlet, whereas a no-slip condition was imposed on the wing surface. Periodic boundary conditions were imposed on the vertical

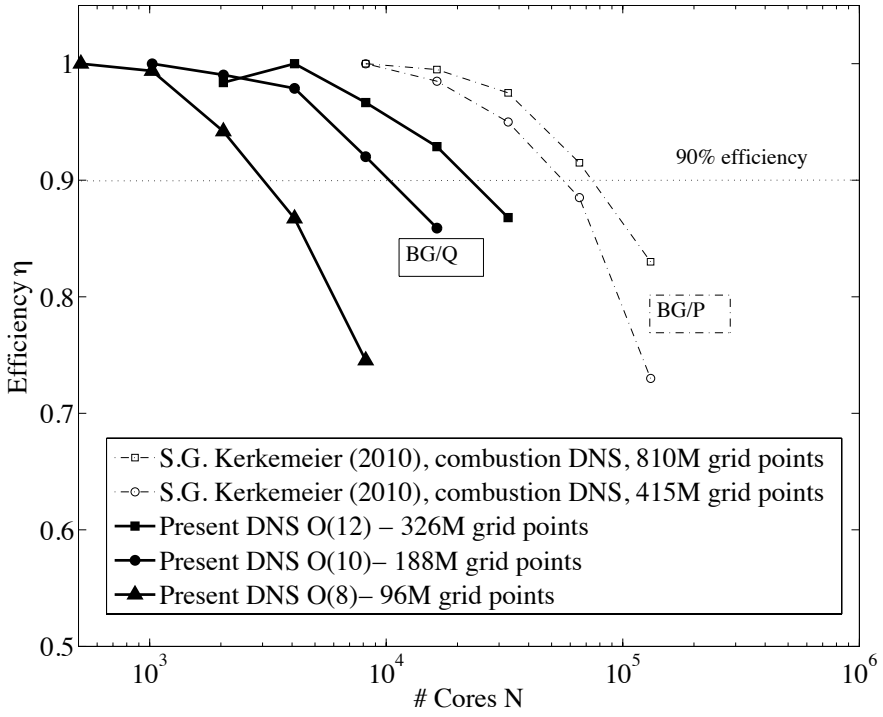

Figure 2: Scalability tests of NEK5000 as function of number of grid points

side planes of the domain. The total height of the DNS domain was 0.25c, with 0.5c in the wake. The span was reduced to 0.05c. The domain of the RANS calculation corresponds to the dimensions of the experimental test section of the hydrodynamic tunnel at IRENav.

The spectral mesh was determined using the following method: having restricted the domain to the near wall region, the spatial resolution was determined using the wall friction from the RANS calculations, according to the general requirements for a DNS at $Re = 450,000$, namely

$\Delta y_{min} < 0.2$,$\Delta x_{max} = \Delta z_{max} < 10$. Then, the span length was set according to the computational time allocated for the project, i.e. 0.05c. It is important to point out that the reduced span can force development of 3D boundary layer flow in the transition region, related to the development of "hairpin structures". Although the influence of Reynolds number on the transverse wavelength has not been fully characterized in the literature, a direct dependence has been shown in the experiments of [4] on a sd7003 airfoil. They show first that LSB thickness linearly depends on boundary layer thickness. They also show that the transverse wavelength of what they call C-shape structures is approximately 0.2c at $Re = 20,000$, compared to about 0.1c at $Re = 60,000$. It is then reasonable to estimate that this parameter may be proportional to the boundary layer thickness in the proximity of the LSB, i.e a laminar boundary layer thickness, which is proportional to $1/\sqrt{Re}$. Using the current Reynolds number of $Re = 450,000$, this gives an estimation of about $0.04c$ for the transverse wavelength of hairpin structures, so $0.05c$ was considered a minimum for the present study.

The spectral mesh is shown in figure 4. It is refined close to the wall to obtain a low y^+ value, whereas it is almost constant in the x (chordwise) and z (spanwise) directions. This leads to 188480 spectral elements, leading to approximately O(8) at $Re = 225,000$ (mesh sensivity analysis) and O(12) at $Re = 450,000$ (study case).

To obtain the DNS, a progressive increase of the element order was performed to advance in time, up to the target mesh. As the DNS code is semi-implicit, it requires the local CFL number to be strictly $CFL = u\Delta t/\Delta x < 0.75$. The computations were carried out with $CFL \approx 0.5$.

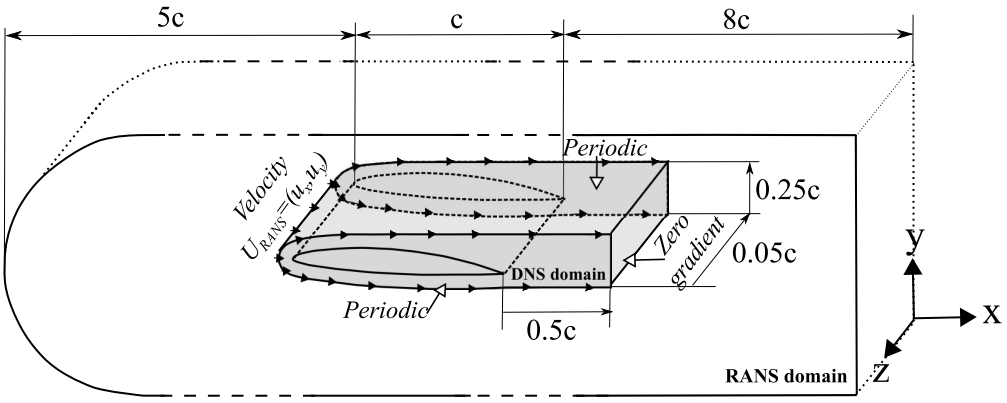

Figure 3: Computational domain of the NACA66 hydrofoil.

307

308 *3.3. Isotropic von Kármán turbulence model*

309 In order to add the perturbation at the inlet of the computational do-
310 main, an isotropic von Kármán turbulence model ([23]) was implemented
311 into the NEK5000 code. This model is based on the energy spectra of the
312 perturbations. The energy spectrum is set numerically by using random
313 number-generating algorithms [31] to generate random angles, resulting in a
314 randomized field. The von Kármán isotropic turbulence model considers the
315 linear velocity and the angular velocity components of the disturbances as
316 spatially varying stochastic processes and specifies power spectral density to
317 each of them.

318 For this study, a modified von Kármán spectrum was utilized:

$$E(\kappa) = c_E \frac{u_{rms}^2}{\kappa_e} \frac{(\kappa_1/\kappa_e)^4}{[1+(\kappa_1/\kappa_e)^2]^{17/6}} e^{[-2(\kappa_1/\kappa_\eta)^2]} \tag{2}$$

319 Here, $\kappa_1=(\kappa_i\kappa_i)^{1/2}$ and $\kappa_\eta=\epsilon^{1/4}\nu^{-3/4}$ are obtained from the kinetic energy

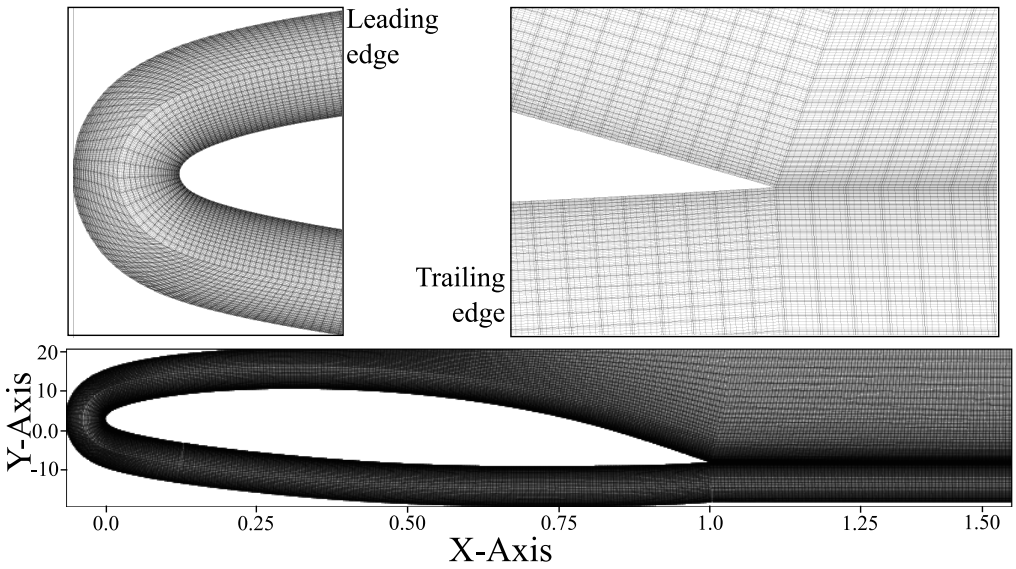

Figure 4: Spectral element mesh of the NACA66 hydrofoil, $N = 188,480$.

by integrating the energy spectrum over all the wave numbers, and then utilizing the gamma functions. κ_e is linked to the smallest wave number, and c_E is a constant. The mathematical details and derivations can be found in [18], and details about the von Kármán spectra used here can be found in [7].

The von Kármán model is applied only to a portion of the inlet domain but covers the entire hydrofoil boundary layer. The disturbances are convected downstream by the free-stream flow, destabilizing the boundary layer and triggering the turbulence. The integral length scale is set to 0.006c, corresponding to 50% of the boundary layer thickness in the transition region, whereas the smallest scale corresponds to the smallest cell at the inlet, i.e. 0.0018c.

3.4. Sensitivity analysis

A sensitivity analysis was performed for a lower Reynolds number ($Re = 225,000$) for element orders from O(6) to O(10). The effect of mesh resolution was investigated in the unsteady region of the LSB where vortex shedding occurs, and in the turbulent region. After selecting the required resolution, the element order was increased to simulate the higher Reynolds number ($Re = 450,000$), assuming that the LSB dynamics would be similar.

First, the flow in the transition region was analyzed. Figure 5 shows the instantaneous velocity field in the unsteady region of the LSB. Although the figures cannot be directly compared, since they were taken at different instants with different mesh resolutions, their prediction of the LSB shedding process can be qualitatively compared. The lower order mesh (O(6)) is clearly too coarse to capture the LSB vortex shedding correctly. Numerical instabilities disturb the unsteady region of the LSB, resulting in the formation of smaller structures, and hence further numerical instabilities form downstream. From order O(8), this numerical effect seems to be suppressed and the shedding process is correctly captured.

This observation is confirmed in Figure 6(a), which shows the pressure spectra downstream from the LSB. Due to numerical instabilities, the O(6) produces a pressure peak at 125 Hz compared to 85 Hz for O(8) and O(10). The effect of mesh resolution on the development of turbulence is also observed near the trailing edge. The spectra of streamwise velocity V_X clearly shows that increasing element order tends to capture a larger range of turbulent scales, as indicated by the frequency range over which the slope is

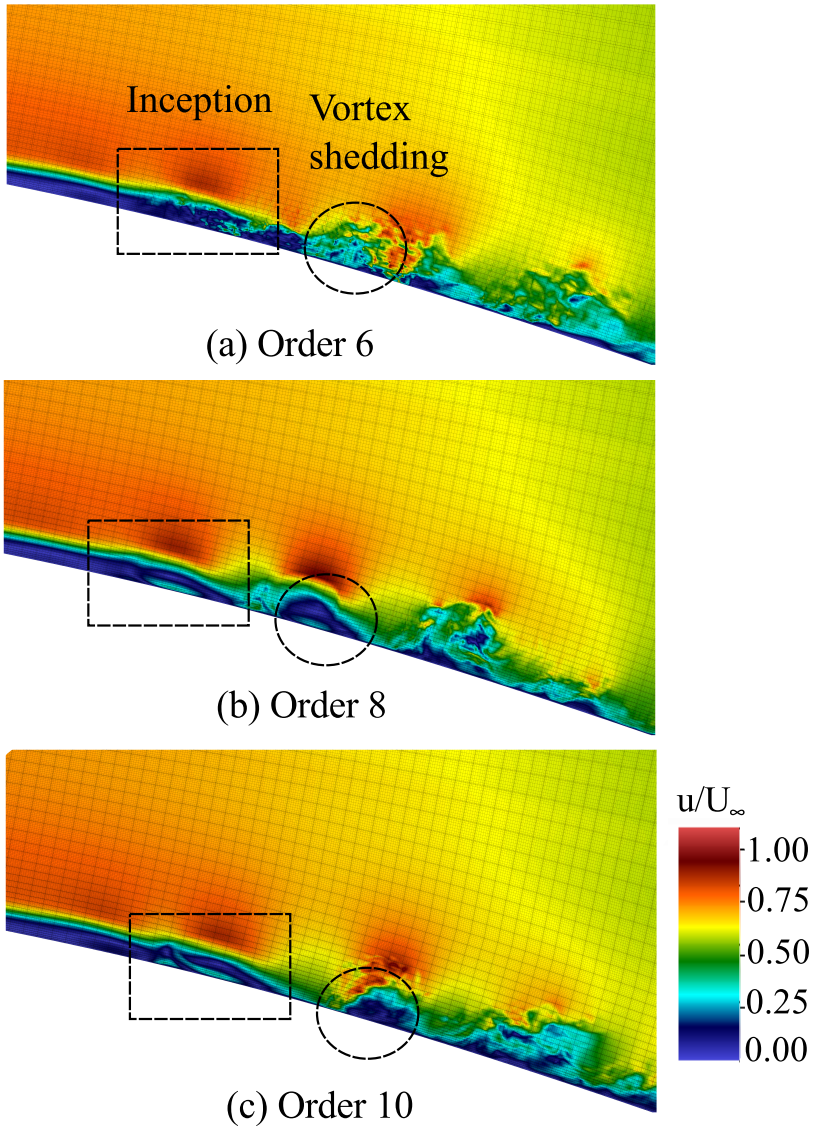

Figure 5: Convergence of the LSB shedding. Velocity contours downstream of the LSB for three different element orders, $Re = 225000$.

Element order	C_L	C_D
O(6)	0.8198 ± 0.055	0.0213 ± 0.0049
O(8)	0.8272 ± 0.061	0.0219 ± 0.0034
O(10)	0.8274 ± 0.062	0.0215 ± 0.00057

Table 1: Convergence of lift and drag coefficients as a function of the element order, $Re = 225000$.

-5/3, corresponding to the characteristic slope of turbulent cascade. Since the primary objective of the present paper is to investigate LSB dynamics, it is not necessary to achieve convergence on the turbulent spectra.

Finally, the effect of element order on components of hydrofoil performance was tested, see Table 1. It was observed that drag converged for all mesh resolutions, whereas lift is slightly under-predicted for the lower order O(6) mesh, as compared to the O(10) mesh.

According to this convergence study, at $Re = 225,000$ the mesh with order O(8) is sufficient to fully capture the LSB dynamics, and the transition to turbulence. The total number of points was $N = 96,501,760$. The element order was then increased to 12 to simulate the case at $Re = 450,000$. Figure 7 shows the final mesh resolution along the chord for the two Reynolds numbers at the wall in the tangential, normal and spanwise directions, respectively. It is taken from the friction velocity, which is time and spanwise averaged. Because of the non-uniform distribution of the spectral nodes, Δx^+ and Δz^+ present maximum and minimum values, which are taken from the largest and smallest cells within one spectral element. This corresponds to the maximum resolution as it is at the wall, and because the spectral ele-

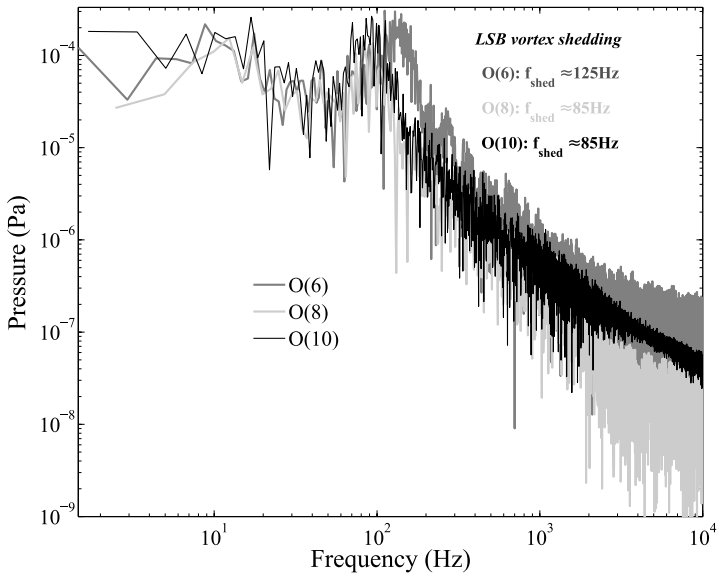

(a) Pressure spectra at $x/c = 0.8$

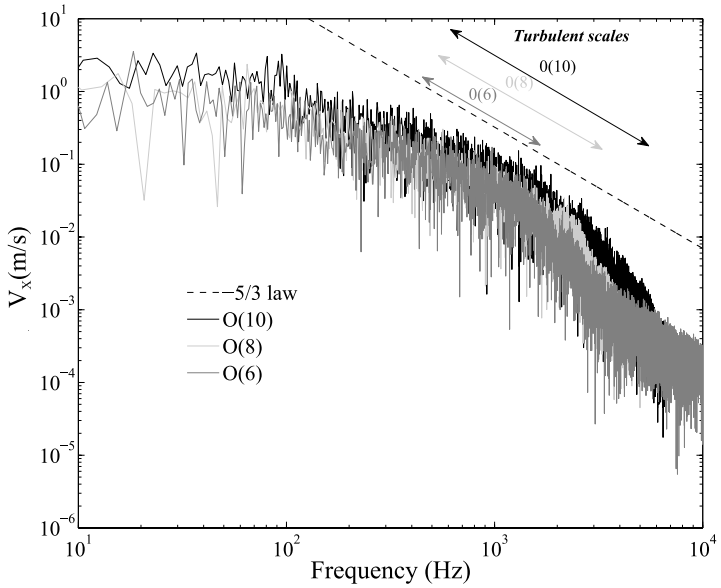

(b) Spectra of Vx at $x/c = 1.0$

Figure 6: Effect of element order on (a) LSB vortex shedding and (b) turbulent scales, $Re = 225000$.

ments are uniformly distributed through the domain along the x and z axes. The final resolution for O(8), $Re = 225000$ leads to $\Delta x^+_{max} = \Delta z^+_{max} = 3$ and $\Delta y^+_{min} = 0.1$, and for O(12) it is $\Delta x^+_{max} = \Delta z^+_{max} \approx 7$ and $\Delta y^+_{min} = 0.2$, corresponding to 326 million grid points at $Re = 450000$. Even though the mesh resolution is lower for the higher Reynolds number, it is considered to be sufficient for analyzing the transitional flow. As a comparison, a similar method was recently presented in [19] for a DNS around a wing section at a similar Reynolds number ($Re = 400,000$), using Nek5000 on a NACA4412 over a full domain. This study obtained 3.2 billion grid points with strong wall refinements, to obtain approximately the same mesh resolution.

4. Results and discussion

4.1. Mean flow analysis: DNS at Re=450,000

To check the validity of the RANS velocity boundary conditions of the DNS domain, the mean flow obtained with DNS was compared to the transitional RANS calculations. The velocity fields are shown in Figure 8. Good agreement is observed overall. The stagnation at $x/c = 0.0055$ is correctly predicted by DNS, and the velocity gradient is reproduced in the DNS up to the LSB, after which point differences are observed because the RANS solver does not capture the LSB unsteadiness.

Local velocity profiles along the chord are shown in Figure 9. Good agreement is observed within the boundary layer; however the DNS calculates higher external velocities (by approximately 5%) compared to the RANS calculation, due to added confinement. This numerical error is corrected in

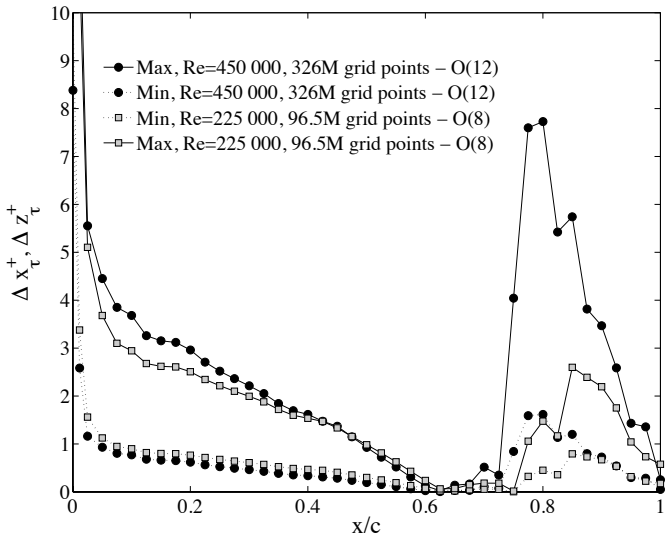

(a) Streamwise (x-axis) and spanwise (z-axis) directions

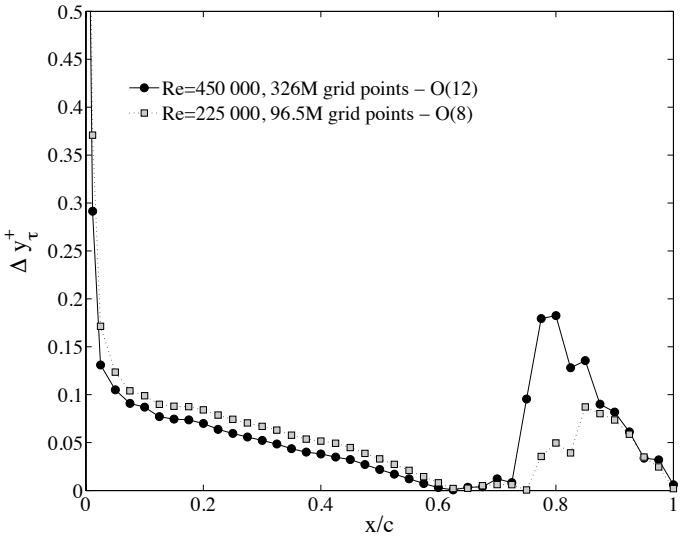

(b) wall normal direction (y-axis)

Figure 7: Mesh resolution at the hydrofoil surface for the two cases considered

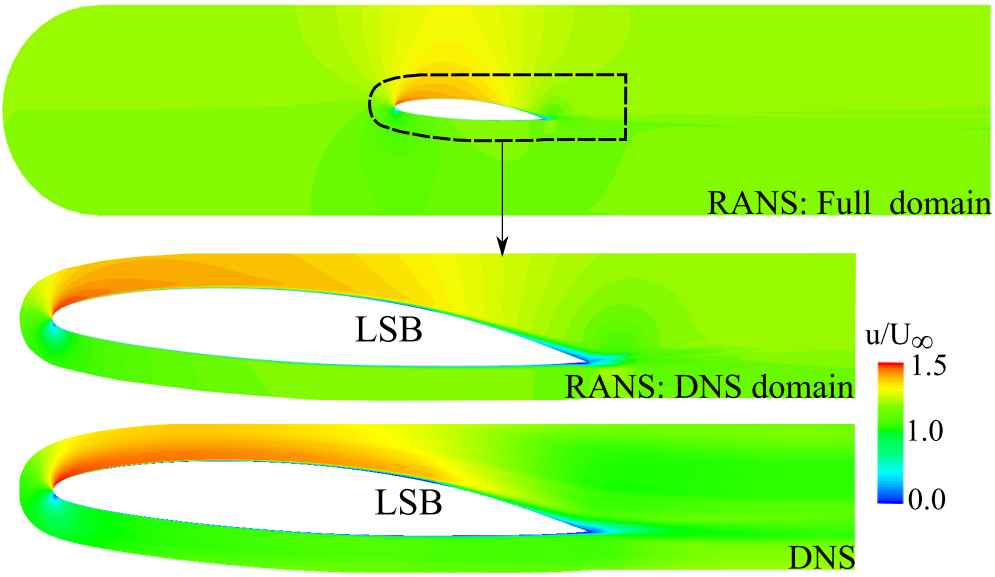

Figure 8: Comparison of the RANS and DNS velocity fields, Re=450,000.

the results section, to ensure that the pressure coefficient calculations and the shedding frequencies compare with experimental values. As expected, the velocities are the same at the upper boundary as RANS velocity profiles are imposed in the DNS calculations.

The method was tested for the lower Reynolds number case at Re=225,000, which was used for the sensivity analysis. As shown in Figure 10, the DNS calculation of external boundary layer velocities was greater than for the higher Reynolds number, at 8%. This difference is attributed to the increase in boundary layer thickness, which magnifies the confinement effects.

Table 2 compares the LSB characteristics between RANS and DNS. Since DNS captures the velocity gradient well, its calculation of laminar separation

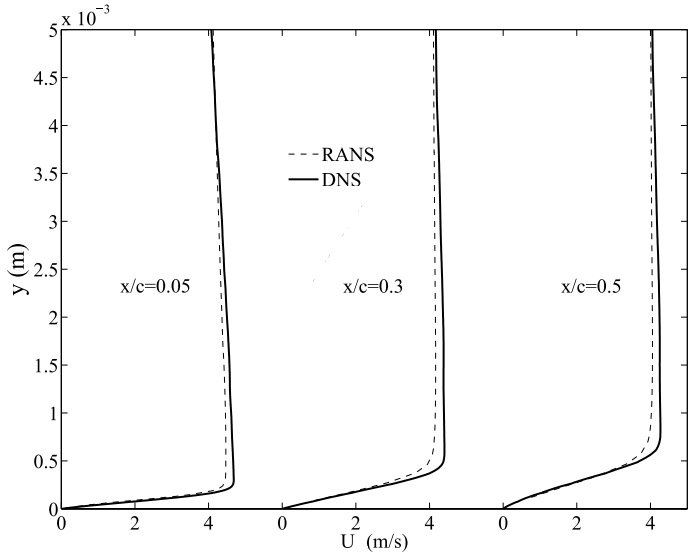

Figure 9: Comparison of the RANS and DNS velocity profiles for three different locations, Re=450,000.

is very close to the RANS value. It can be seen that the LSB vortex shedding frequency obtained from DNS (f_{shed}) compares well with the experimental value ($f_{exp-shed}$) extracted from wall pressure measurements. This is consistent with the work of [33], which used the Strouhal number, $St_\theta = \frac{f_{shed}\theta_{sep}}{u_{sep}}$, to characterize the shedding frequency, considering it to be dependent only on the boundary layer quantities at the laminar separation, captured numerically by DNS. The computed Strouhal number is $St_\theta = 0.0090$ for $Re = 450,000$, as compared to $St_\theta = 0.0068$ found by [33]. This difference is attributed to the different case studied by [33], namely a flat plate submitted to a pressure gradient.

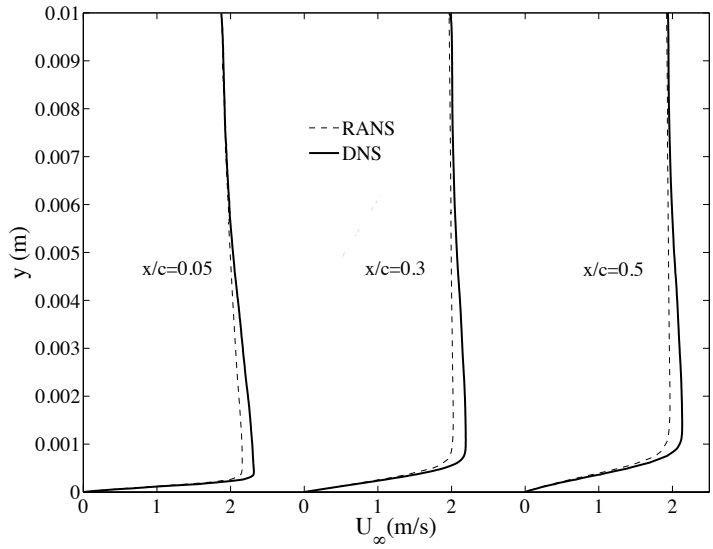

Figure 10: Comparison of the RANS and DNS velocity profiles for three different locations, Re=225,000.

Case	x_{sep}	x_{re}	f_{shed}(Hz)	$f_{exp-shed}$(Hz)
DNS - Re=450,000	0.62	0.72	335	300
RANS - Re=450,000	0.65	0.72	-	-

Table 2: Comparison of RANS and DNS LSB characteristics. x_{sep} and x_{re} are the laminar separation and turbulent reattachment location, f_{shed}(Hz) and $f_{exp-shed}$ are the numerical and experimental shedding frequencies.

4.2. Investigation of pressure fluctuations: experiments vs DNS at Re = 450,000

Experiments in the cavitation tunnel were first performed at $\alpha = 4°$ for $U_\infty = 1.5$ m/s to 10 m/s in steps of 0.5m/s. The results are shown in Figure 11, where frequency spectra of wall pressure at $x/c = 0.7$ and $x/c = 0.8$ are plotted for all the velocities considered. To illustrate the evolution of wall pressure fluctuations with the LSB dynamics, Figure 12 shows the average position of the LSB (in blue), the region of LSB vortex shedding where periodic fluctuation occurs (in green), and the fully turbulent region (in red), as the upstream velocity increases.

First, it is observed that the frequency of LSB shedding increases linearly as Reynolds number (i.e. U_∞) increases, from about 100 Hz for $U_\infty = 1.5$m/s, up to about 1000 Hz for $U_\infty = 7$m/s. The evolution of this frequency from $x/c = 0.8$ to $x/c = 0.7$ visible in Figure 11 illustrates the displacement of the LSB along the leading edge. The frequency peak vanishes after $U_\infty > 3.5$m/s at $x/c = 0.8$ (Figure 11 (b)) and appears starting $U_\infty > 4$m/s at $x/c = 0.7$ (Figure 11 (a)), which clearly means that periodic fluctuation due to LSB shedding move toward the leading edge. Figure 12 illustrates that this variation (in green) is primarily due to the decrease in LSB size (U_∞ <4m/s to 4m/s< U_∞ < 8m/s), which is due to an increase in Reynolds number. Secondly, a decrease in viscous effects slightly increases the adverse pressure gradient, which tends to shift the LSB toward the leading edge. The trailing edge vortex shedding frequency identified in the dotted area is illustrated in Figure12 at $U_\infty > 8$ m/s. Due to a large displacement of the LSB toward the leading edge and the early establishment of turbulent boundary layer in

a relatively strong adverse pressure gradient region, the turbulent boundary layer tends to detach at the trailing edge for the highest velocities, although the wall friction increases. This phenomenon had been investigated numerically previously, in [11]; in this study, an abrupt transition to turbulent flow caused by a leading edge LSB was associated with the sudden generation of a vortex at the trailing edge, caused by detachment of the turbulent boundary layer (see also Figure 12 at $U_\infty > 8$m/s, in orange). Finally, the additional frequencies around 400Hz for 4.5m/s$< U_\infty <$ 8m/s are natural vibrations of the hydrofoil excited by LSB vortex shedding, which are not investigated in this paper.

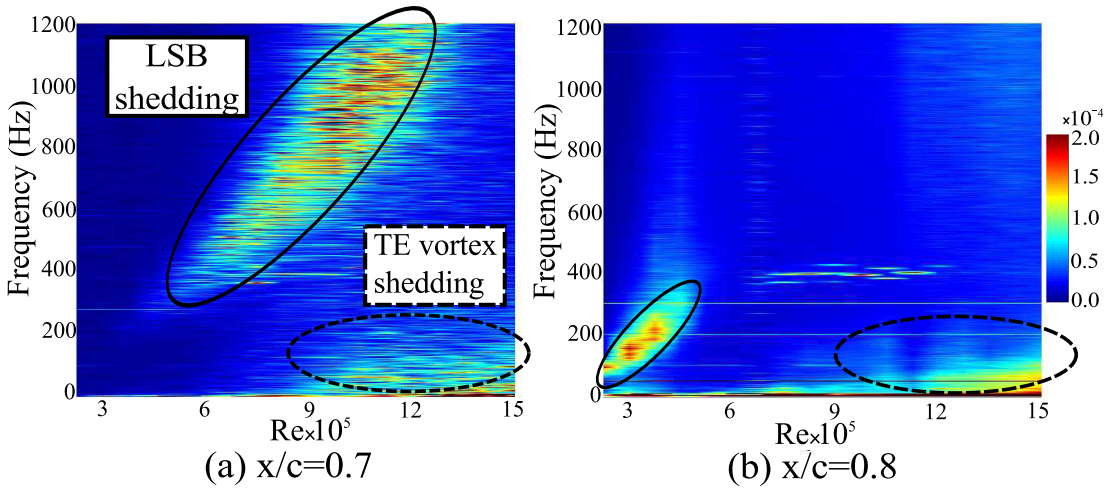

Figure 11: Experimental frequency spectra of wall pressure at (a) x/c=0.7 and (b) x/c=0.8 as function of Reynolds number, $\alpha = 4°$.

Figure 13 compares the local wall pressure coefficients measured experimentally to those obtained with DNS at $Re = 450,000$, $U_\infty = 3$m/s, for

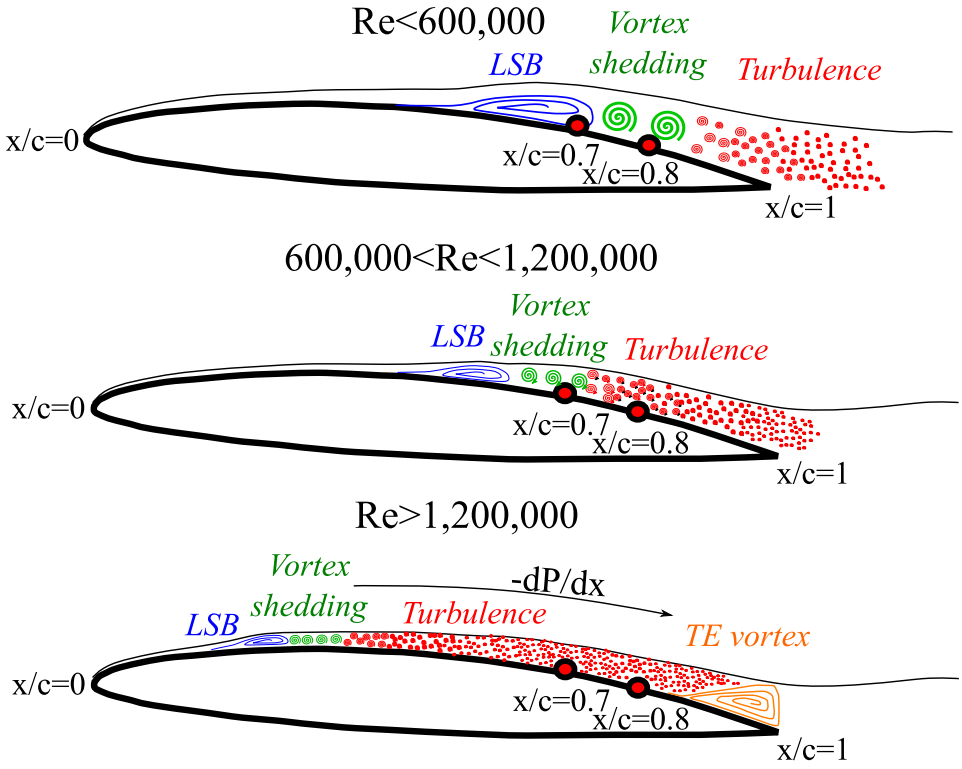

Figure 12: Evolution of LSB dynamics with the Reynolds number. TE=trailing edge.

$x/c = 0.7$, $x/c = 0.8$ and $x/c = 0.9$. The full DNS is plotted in time, and adjusted temporally to be synchronized with the experimental signal. Overall there is good agreeement between the DNS and experiments, in terms of temporal behavior and amplitudes. In the transition region at $x/c = 0.7$ (Figure 13 (a)), the flow is highlighted by the development of coherent structures and the pressure fluctuations show a strong periodic and intermittent behavior for both DNS and experiments. The amplitudes and modulations are fully captured by the present computations. With the development of turbulence, the pressure signal shows smaller fluctuations with random be-

havior; however the signal is still periodic for $x/c = 0.8$. Near the trailing edge, i.e. at $x/c = 0.9$, the fluctuations are more random with significantly lower amplitudes, clearly demonstrating turbulent fluctuation.

In order to refine the comparison between the measured and predicted wall pressures, a fast fourier transform was performed on the signals shown in Figure 13. The results are shown in Figure 14. Again, there was good agreement between DNS and measurements for all spectra. At $x/c = 0.7$, DNS captures the main frequency peak of LSB vortex shedding, with good agreement in both amplitude and frequency range. A secondary peak around 500Hz is also observed, resulting from intermittency. At higher frequencies, there is a rapid decay in amplitude. At $x/c = 0.8$ and $x/c = 0.9$, the main peak is still observed, but with a progressive reduction in amplitude, as also observed in experiments. Moving closer to the trailing edge, an increase in amplitude at higher frequencies is observed, due to development of turbulence. Again, this matches the experimental data, demonstrating the accuracy of the simulation.

An isosurface of λ_2 (introduced in [20]) is shown in Figure 15 for $0.6 < x/c < 1$, colored with pressure coefficient contours. This figure illustrates a correlation between the evolution of wall pressure, and the boundary layer transition to turbulence. It shows where coherent structures start to form downstream from the LSB, and where the transition to turbulence occurs. Coherent structures associated with the development of TS waves appear at $x/c = 0.65$, which is very close to the point of laminar separation at

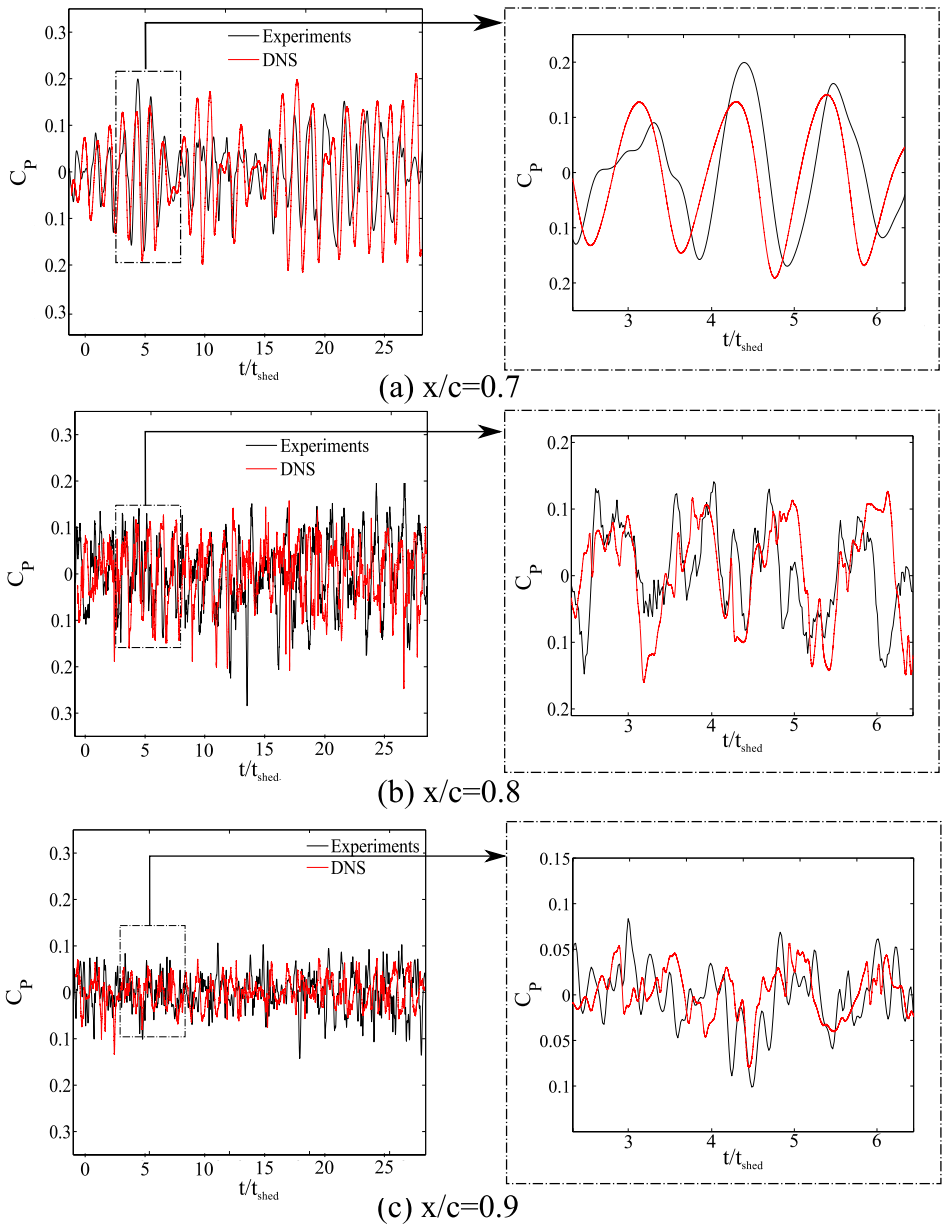

Figure 13: Comparison of computed and measured wall pressure coefficient, $Re = 450,000$, $U_\infty = 3\text{m/s}$

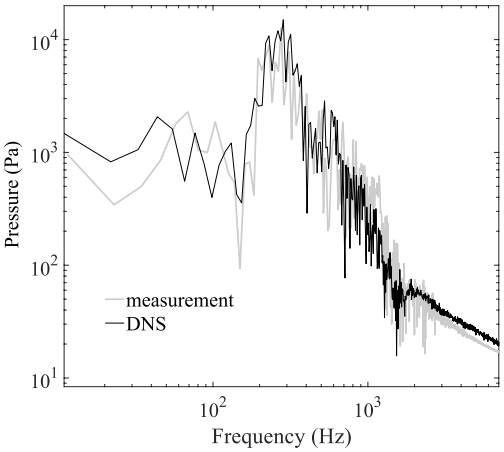

(a)$x/c = 0.7$

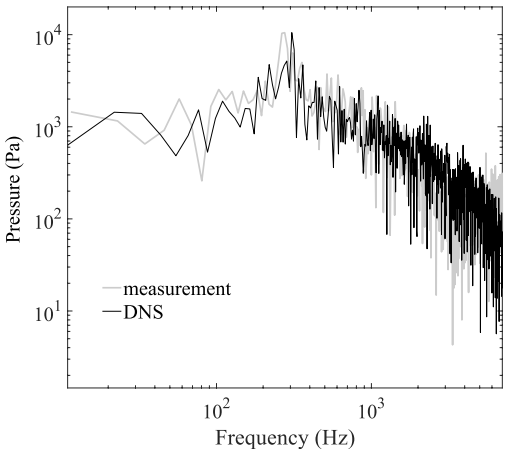

(b)$x/c = 0.8$

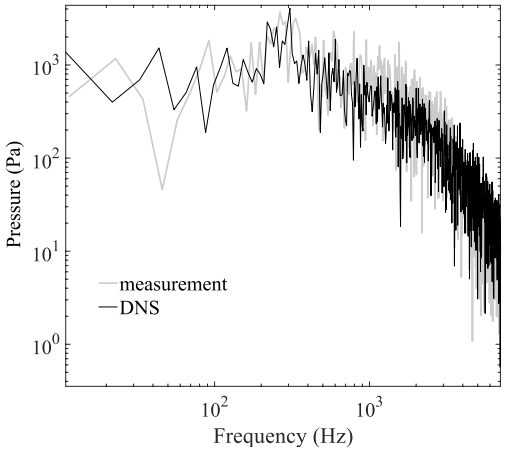

(c)$x/c = 0.9$

Figure 14: Spectral comparison of measured and DNS pressure signals for different chordwise locations, Re=450 000

494 $x/c = 0.62$, see Table 2. The dynamics remain approximately 2D until
495 $x/c = 0.7$. This is consistent with figure 13 (a), which shows that wall pres-
496 sure is fully periodic in this location. In the region $0.7 < x/c < 0.8$, the 2D
497 vortex deforms and breaks down. Coherent structures are still present, in
498 agreement with the periodicity in the pressure signal shown in Figure 13 (b).
499 Subsequently, only turbulent structures are observed up to trailing edge.

While experiments allow a wide range of velocity conditions, they are limited

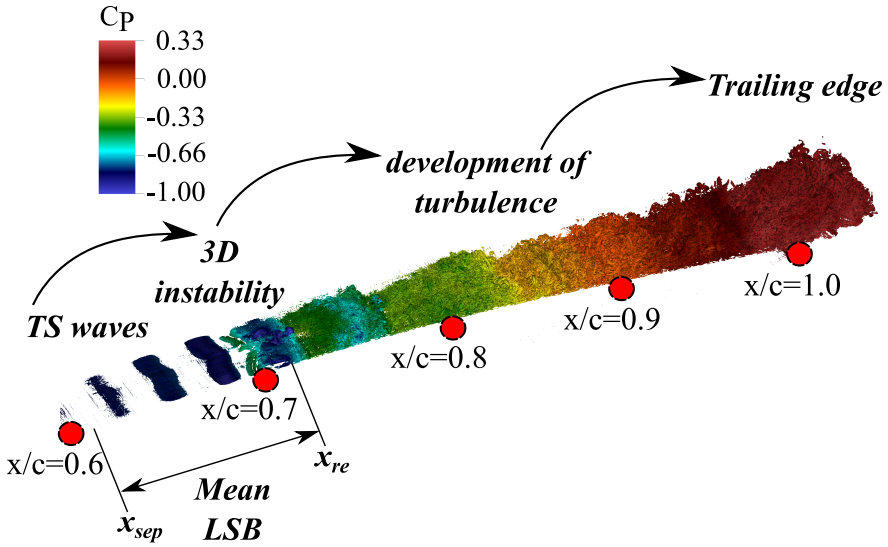

Figure 15: Coherent structures downstream from the LSB, isosurface of λ_2 colored with pressure coefficient, $Re = 450,000$

500

501 spatially to only three points placed in the transition region, and generally
502 only one pressure transducer to record the bubble dynamic. In contrast, the
503 DNS cannot be used to investigate a wide range of Reynolds numbers be-
504 cause of the cost of a single computation, but can offer a complete spatial
505 description of the flow. As such, a complete map of the wall pressure coef-
506 ficients along the chord ($0.6 < x/c < 1$) over 25 periods is shown in Figure

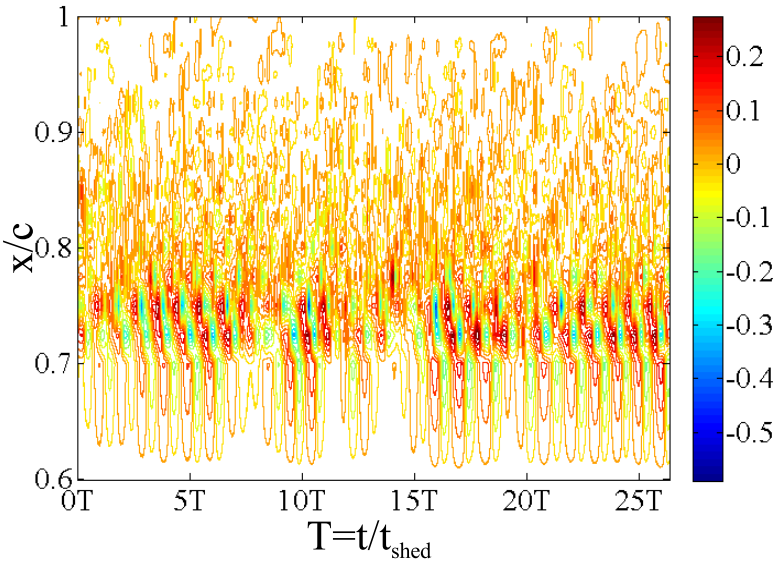

Figure 16: Time evolution of computed wall pressure coefficient fluctuations along the chord of the hydrofoil, Re=450,000

16. Periodic pressure fluctuations appear starting $x/c = 0.62$, i.e. near the laminar separation of LSB. For $0.7 < x/c < 0.75$, the pressure fluctuations increase in amplitude, after which they quickly lose their periodicity, reaching fully turbulent flow after $x/c = 0.85$, in agreement with the numerical observations in Figure 15.

4.3. Analysis of transition behavior: DNS at Re=450,000

Figure 17 shows the instantaneous velocity field and RMS of the spanwise velocity extracted from the mean flow. It is clear that the RMS increases in the unsteady region of the LSB, and is maximum near the turbulent reattachment. It remains high in the transition region, then decreases when turbulence is established. The instantaneous velocity field shows that the

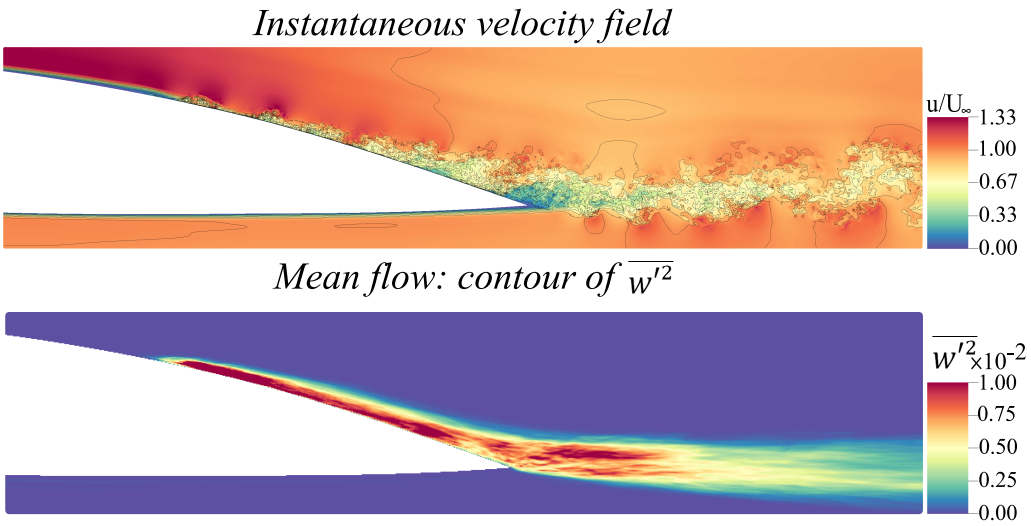

Figure 17: Evolution of unsteadiness downstream from the LSB, Re=450,000

suction side boundary layer increases in thickness with the development of turbulent boundary layer, which interacts with the pressure side boundary layer at the trailing edge to form a turbulent wake instability.

Figure 18 shows the spectra of V_x at three locations along the chord: $x/c = 0.7$, just downstream from the LSB; $x/c = 0.85$, between the transitional and turbulent regions; and $x/c = 1$, in the turbulent region. Velocities were recorded outside of the boundary layer. At $x/c = 0.7$, only the LSB vortex shedding frequency is observed on the spectra. At $x/c = 0.85$, this peak is still observed, and additionally a high amplitude is observed, corresponding to the increased RMS shown in Figure 17. The development of turbulence also leads to the inception of higher frequency components. Finally, at $x/c = 1$, the spectra shows a classical -5/3 slope resulting from the turbulent cascade.

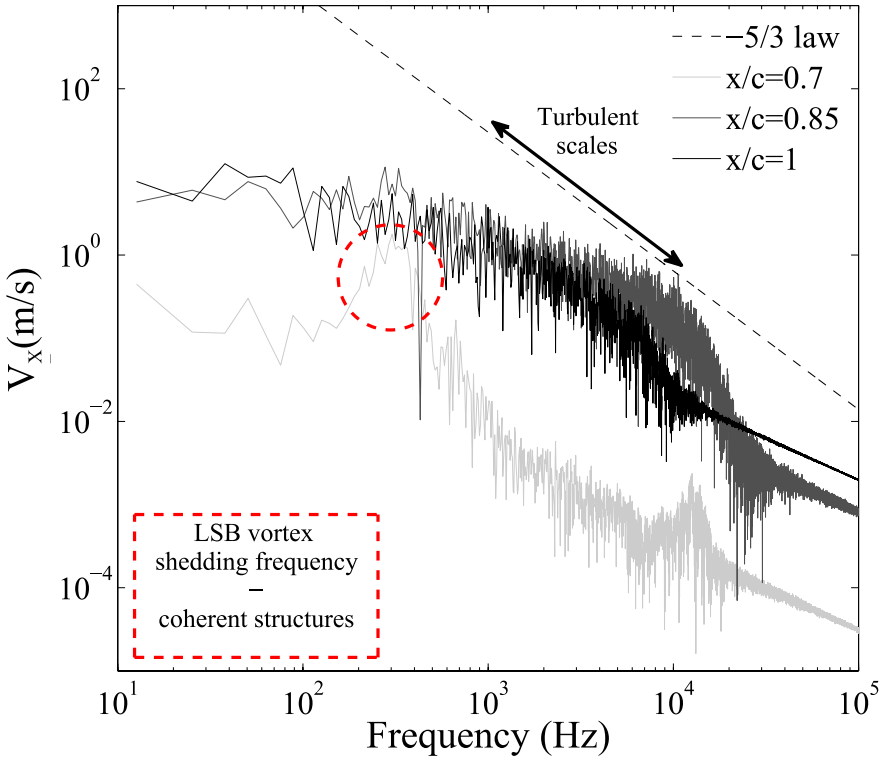

Figure 18: Spectra of V_X for three chordwise locations, Re=450,000

Finally, the transition mechanism for $Re = 450000$ is detailed in Figure 19, which shows the isosurfaces of λ_2 colored with velocity and pressure coefficient contours. The top and bottom subfigures were produced using different values of λ_2 in order to highlight the different mechanisms: development of TS waves for higher λ_2, and development of hairpin structures and turbulence downstream from the LSB for lower λ_2. First, it can be observed on Figure 19(a) that the flow exhibits a typical H-type or K-type transition, as shown for the case of a flat plate with forcing by [35]. The distinction

between these two types of transition cannot be identified in this paper, as only one Λ shape structure was captured spanwise, so it is not possible to determine whether it is aligned (K-type) or staggered (H-type). The top view of Figure 19 shows that TS waves appear downstream from the LSB, and progressively deform with the inception of a 3D instability known as an elliptic primary instability ([28]). The development of this instability leads to the formation of a Λ-shaped structure, also known as a "hairpin" structure, whose breakdown leads to development of turbulent flow. It should be noted that the Reynolds number Re_X at which this transition takes place is comparable to that identified in [35], albeit advanced somewhat due to the angle of attack and the curvature of the hydrofoil: as an example, the TS waves start at $Re = 310000$, compared to $Re = 360000$ for [35]. The velocity field in Figure 19(b) shows that the breakdown of Λ structures is due to development of secondary instabilities, which progressively lead to turbulence. The investigation of the pressure field in Figure 19(c) shows that the pressure is globally maintained (dark blue) during development of the hairpin structure. This means that the vortex convects along the chord with a quasi-constant angular velocity, i.e. it extends the pressure plateau from the LSB region. In the breakdown region, mixing leads to an increase in pressure fluctuations, characterized by more random behavior. In the turbulent region, the pressure increases almost linearly up to the trailing edge.

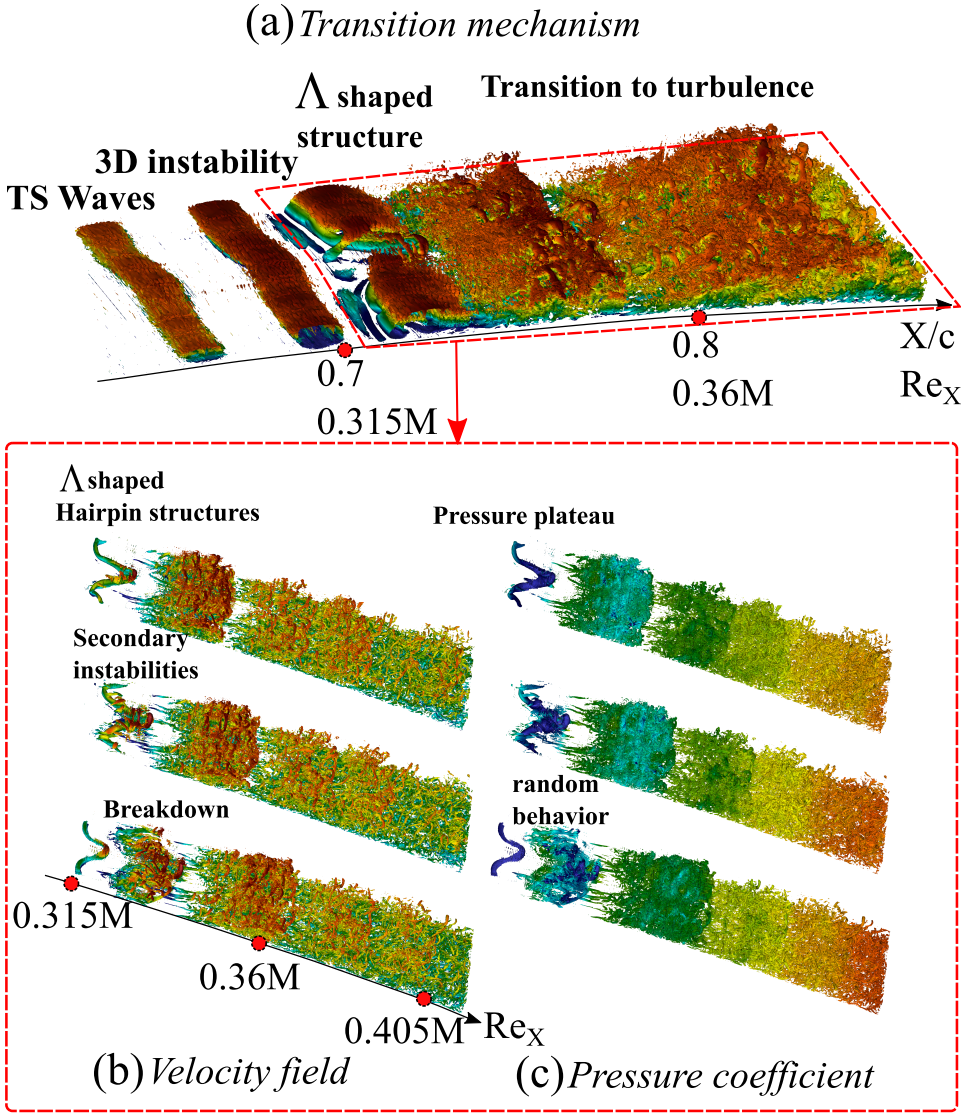

Figure 19: Time evolution of computed wall pressure coefficient fluctuations along the chord of the hydrofoil, isosurfaces of λ_2 colored with velocity contours (top and bottom left) and pressure coefficients contours (bottom right).

5. Conclusion

In this paper, the laminar to turbulent transition and the resulting wall pressure fluctuations were analyzed on a laminar NACA66 propeller section. Despite the moderate Reynolds number investigated ($Re = 450,000$), DNS resolution was successfully obtained by using a simplified fluid domain, which considered the near wall region by imposing RANS velocity profiles at the boundaries. The results were compared with wall pressure measurements performed in a hydrodynamic tunnel.

The DNS correctly reproduced the velocity field as found from transitional RANS calculations, allowing the main characteristics of the LSB to be captured. Experimental investigations of wall pressure fluctuations for a wide range of Reynolds numbers ($225,000 < Re < 1,500,000$) at $\alpha = 4°$ showed that the frequency of vortex shedding downstream from the LSB increases linearly with increasing Reynolds number. Further, the fluctuations move progressively from $x/c = 0.8$ to $x/c = 0.7$, which is associated with a decrease of the LSB length and its shift toward the leading edge. The DNS results for wall pressure fluctuations at $Re = 450,000$ showed good agreement with experiment throughout the different stages, from development of the LSB, through the transition process, up to fully turbulent flow.

Following this validation of the DNS, the interaction between boundary layer flow and the evolution of wall pressure fluctuations was investigated. It was observed that the flow exhibit a classical H-type or K-type transition to turbulence, highlighted by the inception of 2D TS waves, which deform to hairpin structures due to a 3D instability. A secondary instability subsequently causes degradation of the hairpin structures, and the flow transitions quickly

to turbulence. The wall pressures were observed to respond to these different stages of transition:

- from the inception of TS waves at $x/c = 0.65$ to the development of hairpin structures at $x/c = 0.72$, the wall pressures display periodic intermittent behavior with one main period that corresponds to LSB vortex shedding.

- The breakdown around $x/c = 0.75$ has a mixing effect associated with maximum amplitude of wall pressure fluctuations, which subsequently decrease quickly for $0.75 < x/c < 0.8$. Periodic pressure fluctuations are still observed, but with a greater degree of randomness due to multi-scaled structures passing through the local surface.

- In the region of fully developed turbulence ($x/c > 0.85$) the pressure signal reveals random fluctuations of lower amplitude.

It should be noted that because of the complex transitional flow captured, boundary layer flow cannot be fully characterized due to certain numerical effects. From laminar separation up to the inception of TS waves, typical boundary layer flow is reproduced, suggesting the DNS is free of numerical effects, mainly because it is a 2D process. As shown in [33], LSB shedding LSB depends mainly on the boundary layer characteristics at laminar separation, which appear to be correctly predicted by the DNS, as indicated by the comparison of wall pressures with experiments. On the other hand, in the transition region, where secondary instabilities play an important role in the destabilization of the LSB, the numerical setup can strongly influence the development and breakdown of 3D structures. In particular, because of

the reduced span used in the present simulation, it captures only one coherent hairpin structure in the spanwise direction, so the flow may be forced and hence the actual wavelength is probably not fully accurate. This aspect will be investigated in future work by extending the DNS domain size in the normal and spanwise directions. The present setup is also currently used to study fluid structure interaction in transitional flows.

Acknowledgements

This work was performed using HPC resources of GENCI/IDRIS (Grant 2016-[100631]) at Orsay, France on the IBM Blue Gene/Q (Turing). Flow visualizations were made using the open-source software VisIt [6].

References

[1] Astolfi, J.-A., Dorange, P., Billard, J.-Y., Tomas, I. C., 2000. An experimental investigation of cavitation inception and development on a two-dimensional eppler hydrofoil. Journal of Fluids Engineering 122 (1), 164–173.

[2] Baltazar, M., Rijpkema, D., Falco de Campos, J., 2017. On the use of the $\gamma - re_\theta$ transition model for the prediction of the propeller performance at model scale. In: Proceeding of the Fifth International Symposium on Marine Propulsors, 12nd - 15th June, Helsinki - Finland.

[3] Burgmann, S., Dannemann, J., Schröder, W., 2008. Time-resolved and volumetric piv measurements of a transitional separation bubble on an sd7003 airfoil. Experiments in Fluids 44 (4), 609–622.

[4] Burgmann, S., Schröder, W., 2008. Investigation of the vortex induced unsteadiness of a separation bubble via time-resolved and scanning piv measurements. Experiments in fluids 45 (4), 675.

[5] CARLTON, J., 1994. Marine propellers and propulsion. Butterworths-Heinemann.

[6] Childs, H., Brugger, E., Whitlock, B., Meredith, J., Ahern, S., Pugmire, D., Biagas, K., Miller, M., Harrison, C., Weber, G. H., Krishnan, H., Fogal, T., Sanderson, A., Garth, C., Bethel, E. W., Camp, D., Rübel, O., Durant, M., Favre, J. M., Navrátil, P., Oct 2012. VisIt: An End-User Tool For Visualizing and Analyzing Very Large Data. In: High Performance Visualization–Enabling Extreme-Scale Scientific Insight. pp. 357–372.

[7] Davidson, L., 2011. Fluid mechanics, turbulent flow and turbulence modeling. Chalmers University of Technology, Goteborg, Sweden (Nov 2011).

[8] Delafin, P. L., Deniset, F., Astolfi, J.-A., 2014. Effect of the laminar separation bubble induced transition on the hydrodynamic performance of a hydrofoil. European Journal of Mechanics-B/Fluids 46, 190–200.

[9] Demir, H., Genç, M. S., 2017. An experimental investigation of laminar separation bubble formation on flexible membrane wing. European Journal of Mechanics-B/Fluids 65, 326–338.

[10] Deville, M., Fischer, P., Mund, E., 2002. High-Order methods for incompressible fluid flow. Cambridge University Press.

[11] Ducoin, A., Astolfi, J. A., Deniset, F., Sigrist, J. F., 2009. Computational and experimental investigation of flow over a transient pitching hydrofoil. Eur. J. Mech. B/Fluids 28, 728–743.

[12] Ducoin, A., Astolfi, J. A., Gobert, M.-L., 2012. An experimental study of boundary-layer transition induced vibrations on a hydrofoil. J. Fluids Struct. 32, 37–51.

[13] Ducoin, A., Loiseau, J.-C., Robinet, J.-C., 2016. Numerical investigation of the interaction between laminar to turbulent transition and the wake of an airfoil. European Journal of Mechanics-B/Fluids 57, 231–248.

[14] Eca, L., Lopes, R., Vaz, G., Baltazar, J., Rijpkema, D. ., 2016. Validation exercises of mathematical models for the prediction of transitional flows. In: In: Proceedings of 31st Symposium on Naval Hydrodynamics, 11th-16th September, Berkeley.

[15] Fischer, P., Kruse, J., Mullen, J., Tufo, H., Lottes, J., Kerkemeier, S., 2008. Nek5000–open source spectral element cfd solver. Argonne National Laboratory, Mathematics and Computer Science Division, Argonne, IL, see https://nek5000. mcs. anl. gov/index. php/MainPage.

[16] Gaster, M., 1966. The structure and behaviour of laminar separation bubbles. AGARD CP 4, 813–854.

[17] Genç, M. S., Karasu, İ., Açıkel, H. H., 2012. An experimental study on aerodynamics of naca2415 aerofoil at low re numbers. Experimental Thermal and Fluid Science 39, 252–264.

679 [18] Hinze, J., 1975. Turbulence (2nd edn). New York: McGraw-Gill, 223–
680 225.

681 [19] Hosseini, S. M., Vinuesa, R., Schlatter, P., Hanifi, A., Henningson, D. S.,
682 2016. Direct numerical simulation of the flow around a wing section
683 at moderate reynolds number. International Journal of Heat and Fluid
684 Flow 61, 117–128.

685 [20] Jeong, J., Hussain, F., 1995. On the identification of a vortex. Journal
686 of fluid mechanics 285, 69–94.

687 [21] Jones, L. E., Sandberg, R. D., Sandham, N. D., 2008. Direct numerical
688 simulations of forced and unforced separation bubbles on an airfoil at
689 incidence. J. Fluid Mech. 602, 175.

690 [22] Karasu, I., Genç, M., Açikel, H., 2013. Numerical study on low reynolds
691 number flows over an aerofoil. J. Appl. Mech. Eng 2, 131.

692 [23] Karman, T. V., 1937. The fundamentals of the statistical theory of tur-
693 bulence. Journal of the Aeronautical Sciences 4 (4), 131–138.

694 [24] Karniadakis, G., Sherwin, S., 2005. Spectral/hp element methods for
695 computational fluid dynamics. Oxford science publications.

696 [25] Kerkemeier, S. G., 2010. Direct numerical simulation of combustion on
697 petascale platforms. Ph.D. thesis, ETH Zurich.

698 [26] Koca, K., Genç, M. S., Açıkel, H. H., Çağdaş, M., Bodur, T. M., et al.,
699 2018. Identification of flow phenomena over naca 4412 wind turbine

700 airfoil at low reynolds numbers and role of laminar separation bubble
701 on flow evolution. Energy 144 (C), 750–764.

702 [27] Leroux, J. B., Coutier-Delgosha, O., Astolfi, J. A., 2005. A joint exper-
703 imental and numerical study of mechanisms associated to instability of
704 partial cavitation on two-dimensional hydrofoil. Phys. Fluids 17, 052101.

705 [28] Marxen, O., Lang, M., Rist, U., 2013. Vortex formation and vortex
706 breakup in a laminar separation bubble. J. Fluid Mech. 728, 58–90.

707 [29] Nati, A., De Kat, R., Scarano, F., Van Oudheusden, B., 2015. Dynamic
708 pitching effect on a laminar separation bubble. Experiments in Fluids
709 56 (9), 1–17.

710 [30] Olson, D. A., Katz, A. W., Naguib, A. M., Koochesfahani, M. M.,
711 Rizzetta, D. P., Visbal, M. R., 2013. On the challenges in experimental
712 characterization of flow separation over airfoils at low reynolds number.
713 Experiments in fluids 54 (2), 1–11.

714 [31] Park, S. K., Miller, K. W., 1988. Random number generators: good ones
715 are hard to find. Communications of the ACM 31 (10), 1192–1201.

716 [32] Patera, A., 1984. A spectral element method for fluid dynamics: laminar
717 flow in a channel expansion. J. Comput. Phys. 54, 468–488.

718 [33] Pauley, L. L., Moin, P., Reynolds, W. C., 1990. The structure of two-
719 dimensional separation. J. Fluid Mech. 220, 397–411.

720 [34] Reverberi, A., Lloyd, T., Vaz, G., 2016. Towards cavitation modelling

721 accounting for transition effects. proceeding of the 19th "Numerical Tow-
722 ing Tank Symposium" (NuTTS'16).

723 [35] Sayadi, T., Hamman, C. W., Moin, P., 2013. Direct numerical simula-
724 tion of complete h-type and k-type transitions with implications for the
725 dynamics of turbulent boundary layers. Journal of Fluid Mechanics 724,
726 480–509.

727 [36] Tufo, H. M., Fischer, P. F., 1999. Terascale spectral element algorithms
728 and implementations. In Proceedings of the ACM/IEEE SC99 Confer-
729 ence on High Performance Networking and Computing, Portland, U.S.A.

730 [37] Tufo, H. M., Fischer, P. F., 2001. Fast parallel direct solvers for coarse
731 grid problems. J. Parallel Distrib. Comput. 61 (2), 151–177.

732 [38] Uranga, A., Persson, P.-O., Drela, M., Peraire, J., 2011. Implicit large
733 eddy simulation of transition to turbulence at low reynolds numbers
734 using a discontinuous Galerkin method. International Journal for Nu-
735 merical Methods in Engineering 87 (1-5), 232–261.

736 [39] Visbal, M. R., Gordnier, R. E., Galbraith, M. C., 2009. High-fidelity
737 simulations of moving and flexible airfoils at low reynolds numbers. Ex-
738 periments in Fluids 46 (5), 903–922.

739 [40] Zhang, W., Hain, R., Kähler, C. J., 2008. Scanning piv investigation of
740 the laminar separation bubble on a sd7003 airfoil. Experiments in Fluids
741 45 (4), 725–743.

742 [41] Zhang, W., Samtaney, R., 2016. Assessment of spanwise domain size

effect on the transitional flow past an airfoil. Computers & Fluids 124, 39–53.